PAPER

Optical Pulse Detection IC LIDARX Integrated in MMX-LIDAR

Takahide MIZUNO[†,††a)], ***Member***, **Hirokazu IKEDA**[†], **Hiroki SENSHU**[†††], ***Nonmembers***, **Toru NAKURA**[††††], ***Member***, **Kazuhiro UMETANI**[†††††], ***Nonmember***, **Akihiro KONISHI**[††††††], **Akihito OGAWA**[*,**], ***Members***, **Kaito KASAI**[*], ***Nonmember***, ***and*** **Kosuke KAWAHARA**[†], ***Member***

SUMMARY LIDARX, an optical pulse detection integrated circuit (IC), has been developed for LIDAR receivers onboard planetary explorers. JAXA developed the IC, based on the experience of the Hayabusa and Hayabusa2 projects, to reduce the circuit size of the receiver, shorten the development period, and improve sensitivity. This IC has been implemented as the core device for the receiver circuit of the LIDAR installed in the explorer of the Japanese Martian Moons eXploration (MMX) mission. The explorer will perform close-up remote sensing and in situ observations of both moons and collect a sample from one of the moons to bring back to Earth. LIDARX is not a simple time-to-digital converter circuit but a sophisticated IC with micro-signal amplification, timing detection, wave height measurement, and clock interpolation functions. Furthermore, LIDARX has a wide dynamic range of 60 dB for light intensity to accommodate distance changes of about three orders of magnitude, which is expected when LIDAR is used as a navigation sensor during landing. The CMOS process is a conventional 0.35 μm, which has been well-tested in high-energy physics, to ensure radiation resistance. This report describes the details, functions, and calibration method of LIDARX's peripheral circuits and the circuits inside the IC, and evaluates its dynamic range and measurement accuracy. In addition, test results are reported for resistance to single-event effects and total ionization dose, which are essential for onboard spacecraft components.

key words: *LIDAR, explorer, MMX, deep space, spacecraft*

1. Introduction

Many probes have been sent to the Moon, planets, and asteroids in recent years to conduct full-scale scientific observations and life exploration. The Moon, in particular, has opened the door to resource exploration, and activities to establish an economic zone are beginning to take place. Many of these spacecraft are equipped with LIDAR (light detection and ranging) for terrain observation and guidance navigation for landers. Examples of LIDAR for terrain observation include LIDAR on the lunar explorer Clementine (1994) [1], MOLA on the Mars Global Surveyor (1996) [2], NLA on NEAR Shoemaker (1996) [3], [4], MLA on Messenger (2004) [5], [6], and LALT on Kaguya [7], [8]. Examples of LIDAR for navigation sensors include the laser rangefinder and laser velocimeter onboard Chang'e-5 [9], [10], which successfully returned samples from the Moon in 2020, and Chandrayaan-3 [11], which successfully landed near the lunar south pole in 2023. The asteroid probe OSIRIS-Rex [12] used a scanning LIDAR for terrain observation [13], [14] and a flash LIDAR for navigation [15], [16]. Meanwhile, for successful sample returns from asteroids, Hayabusa (2003) [17] and Hayabusa2 (2014) [18] used LIDAR both for terrain observation and navigation [19]. In those missions, significant results were also obtained from scientific observations [20], such as measurements of the mass and density of celestial objects.

When a LIDAR system is used both for landing navigation and scientific observation, it will be used over a wide dynamic range spanning tens of meters to tens of kilometers. Similarly, a wide dynamic range is required when the difference between perigee and apogee is large, such as in long elliptical orbits. In the case of sensors for navigation, because only distance is required, waveform saturation in the receiver circuit can be tolerated. In contrast, if reflectance measurements of planetary surfaces are required for scientific observation, it is necessary to maintain the linearity of the wave height measurement in the receiver circuit. A change in distance from a few tens of kilometers to a few tens of meters produces a change in the optical energy of the reflected wave of up to 60 dB. Hayabusa's LIDAR employed a charge amplifier as a preamplifier for the receiver, but it had to be partially uncalibrated [17] for the flight due to a lack of development time. Hayabusa2 adopted a hybrid integrated circuit (HIC) integrating an avalanche photodiode (APD) and transimpedance amplifier to shorten the adjustment period owing to its extremely short development time of two years. Thus, waveform saturation had to be tolerated at some altitudes [18].

Based on this experience, JAXA has developed LIDARX [21], a dedicated optical pulse detection IC for LIDAR, in order to reduce the circuit size and shorten the development time of the receiver, and it has been used in the LIDAR installed in the explorer of the Martian Moons eXploration (MMX) mission. LIDARX is connected after the APD and performs amplification, timing detection, and clock interpolation. Time-to-digital converters [22] specially designed to improve time resolution are commercially

Manuscript received May 7, 2024.
Manuscript revised August 6, 2024.
Manuscript publicized December 12, 2024.
[†]JAXA, Sagamihara-shi, 252–5210 Japan.
[††]The Graduate University for Advanced Studies, SOKENDAI, Sagamihara-shi, 252–5210 Japan.
[†††]CIT, Narashino-shi, 275–0016 Japan.
[††††]Fukuoka Univ., Fukuoka-shi, 814–0180 Japan.
[†††††]Okayama Univ., Okayama-shi, 700–8530 Japan.
[††††††]Chiba Univ., Chiba-shi, 263–8522 Japan.
[*]IHI Aerospace, Tomioka-shi, 370–2398 Japan.
[**]Tokai Univ., Hiratsuka-shi, 259–1292 Japan.
a) E-mail: mizuno.takahide@jaxa.jp
DOI: 10.1587/transele.2024ECP5028

available as dedicated ICs for LIDAR. Examples include ams OSRAM's AS6500 and Texas Instrument's TDC7201. Several excellent time-to-digital converters have been proposed [23], [24] for the ROIC (readout IC) of the focal plane array for LIDAR using Geiger-mode APD. These circuits were proposed based on the assumption of a digital signal level or a large current from the Geiger-mode APD, and do not have amplification and timing detection functions for small signals. Therefore, it is necessary to implement additional analog circuits to amplify the small signals from the APDs, as well as circuits to detect the timing of the signals and output them at the digital level. If wave height measurement is required, a peak hold circuit is also needed separately. LIDARX is a high-functionality IC that can accommodate all of these functions on a single chip and support a wide dynamic range. It is difficult to use the latest semiconductor process for ICs to be mounted in space because of the effects of radiation. In addition, the circuitry surrounding the IC is also limited in terms of the board design and components that can be used, making it difficult to use high-speed clocks. LIDARX is a high-functionality IC that combines all of these functions on a single chip and is capable of handling a wide dynamic range.

The remainder of this report is organized as follows. Section 2 describes the orbits and LIDAR observations in the MMX mission. Sections 3–7 provide details of LIDARX and its evaluation equipment, calibration methods, measurement accuracy, and radiation tolerance. Finally, Sect. 8 gives an overview of the packaging and quality conformance inspection of the flight model.

2. LIDAR Observation in MMX

JAXA is planning MMX [25] to explore Phobos, a Martian moon. During this mission the spacecraft will be injected into orbit around Mars with the same orbital period as Phobos. The quasi-satellite orbit (QSO) is not an ellipsoid with Phobos as one focus, but rather a Phobos-centered ellipsoid with an axis ratio of about 1 : 2. The highest QSO is 100 km × 198 km and the lowest is 20 km × 27 km. The explorer will orbit Mars for about three years, landing on Phobos up to two times to collect surface materials that may be of Martian origin.

The satellite's orbit can be corrected with high accuracy by comparing the surface profile of Phobos with the results of continuous LIDAR measurements along with orbit prediction and attitude information obtained from its star-tracker camera. In addition, continuous distance measurements by LIDAR during landing descent operations will provide important information on the density distribution of Phobos. For these observations, the LIDAR onboard the explorer is required to perform distance measurements at altitudes ranging from 100 km to 100 m, and it needs to have albedo measurement capabilities for surface material exploration [26].

To perform the observations described above, a very simple estimate of the amount of received charge is made. Assuming the surface of the object to be a Lambertian target, the amount of charge output from the APD for distance measurements at distance R is given by

$$Q_r = \frac{\tau D_r^2 \rho_t}{4R^2} \eta M e \frac{\lambda E_t}{hc} \times overlap(R), \tag{1}$$

where τ, D_r, R, E_t, ρ_t, η, M, e, h, c and λ are the transmissivity of the optics, diameter of the receiver optics, range, transmission energy, target surface albedo, quantum efficiency of the APD, multiplication factor of the APD, elementary charge, Planck's constant, the speed of light, and the laser wavelength, respectively. Moreover, $overlap(R)$ is the ratio of overlap of the fields of view of the transmitting and receiving systems.

If the combined efficiency of the transmitter and receiver optics is taken as $\tau = 0.6$, the aperture of the receiver telescope as $D_r = 127$ mm, the transmission energy as $E_t = 20$ mJ, the reflectance of Phobos's surface as $\rho_t = 0.05$, the APD multiplication factor as $M = 100$, the APD quantum efficiency as $\eta = 0.36$, the transmitting laser wavelength 1.064 µm, and the overlap ratio as $overlap(R) = 1$, then the charge obtained when ranging at a distance $R = 100$ km is 7.5 fC. On the short-range side, measurement at 100 m is required, and the amount of charge at that time is 7.5 nC. Therefore, the receiver circuit is required to maintain linearity for the amount of charge with a dynamic range of 60 dB, assuming a minimum detectable charge of 7.5 fC.

However, LIDAR always requires improvement of the resolution of distance measurements. Hayabusa2's LIDAR achieved a distance measurement resolution of 50 cm with a clock equivalent to 300 MHz, and the MMX LIDAR is required to have a resolution of about 10 cm. Therefore, a sub-nanosecond resolution is required for time measurements.

3. Optical Pulse Detection IC LIDARX

3.1 Circuit Overview

To reduce the circuit size and shorten the development time of the receiver, we have developed an application-specific integrated circuit (ASIC) to provide gain control for a wide dynamic range of 60 dB and a high temporal resolution of about 10 cm, as required by the LIDAR. This IC is a dedicated analog ASIC device based on submicron analog IC technology developed systematically in the field of high-energy physics. The fabrication process is a 0.35-µm CMOS bulk process, and the chip size is 3 mm × 3 mm. The supply voltage externally supplied to the IC is ±1.65 V. The circuitry of the IC is essentially grounded at −1.65 V, which is the potential of the substrate, and is connected to external ground at an intermediate potential of 0 V.

The circuit that introduces the signal from the photosensor APD to the IC and the circuit inside the IC are outlined in Fig. 1. The power supply and control lines are omitted because they would complicate the diagram. The received light pulse is converted into a current pulse by the APD. The amount of charge on the current pulse varies inversely with

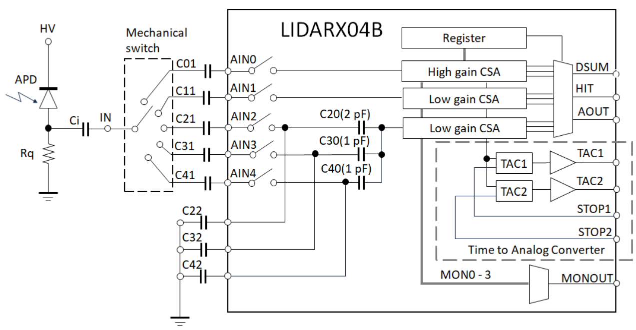

Fig. 1 Schematic of LIDARX.

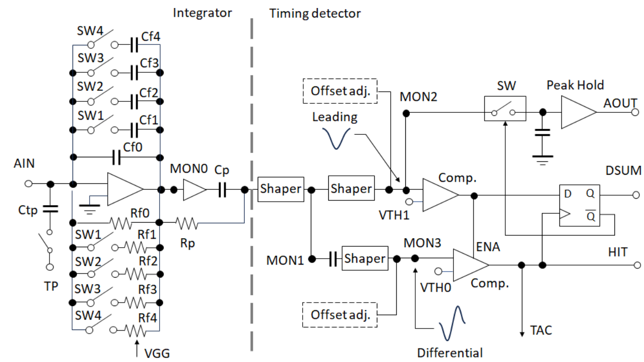

Fig. 2 Schematic of the charge-sensitive amplifier.

the square of the distance, so it is divided into five channels (CH0–CH4) according to the amount of charge. CH0 is the long-distance channel with the highest gain, and CH4 is the short-distance channel with the lowest gain. The five channels are designed to have the capability to handle large charge changes by combining two types of charge-sensitive amplifiers and three types of charge-splitting ratios. The charge-sensitive amplifier module provides gain adjustment, timing detection, and wave height measurement. The detected timing is used by the time-to-analog converter (TAC) circuit to interpolate the clock for time measurements.

3.2 Charge Splitting

LIDARX has five channels corresponding to different electron charge levels. The input pins corresponding to the five channels are AIN0–AIN4. The APD and IC are AC coupled by capacitor Ci to isolate offset variations. Mechanical relays with low thermal noise are recommended for switching signals from the APD. Semiconductor switches such as multiplexers should be avoided, especially for CH0 and CH1, where minute amounts of charge need to be amplified.

CH0 and CH1 input the signal directly to the charge-sensitive amplifier module without charge splitting, while CH2, CH3, and CH4 are used when the signal charge is excessive at relatively short distances. In these channels, the charge is reduced by the capacitance ratio between the capacitor connected externally and the capacitor inside the IC, after which it is input to the charge-sensitive amplifier. Specifically, in the case of CH2, the amount of charge entering from AIN2 via C21 is split into C20/(C20 + C22) before being input to the low-gain charge-sensitive amplifier (CSA). As shown in the next section, the right side of C20 is virtually grounded by feedback from the operational amplifier. Thus, LIDARX requires switching of the input by a mechanical relay and charge splitting by an externally connected capacitor. On the evaluation board reported here, C22, C32, and C42 use 16, 256, and 4000 pF, respectively.

3.3 Charge-Sensitive Amplifier

The CSAs used in LIDARX are of two types: high gain with high sensitivity and low gain with relatively low sensitivity. Both types of CSAs have the same internal circuit configuration, but the feedback capacitances Cf0 to Cf4 of the integrator are different.

The time waveform of the output voltage V of the integrator can be approximately expressed by

$$V = \frac{-Q}{C_f} e^{\frac{-t}{C_f R_f}}, \tag{2}$$

where Q is the input charge quantity, C_f is the feedback capacitance, and R_f is the feedback resistance.

Therefore, the voltage wave height V can be adjusted by switching the feedback capacitance C_f. As shown in Fig. 2, gain switching is performed by controlling the switches (SW4, SW3, SW2, SW1) corresponding to the four feedback capacitors Cf1–Cf4 with a 4-bit digital signal. Thus, G0 (0, 0, 0, 0) is the maximum gain and G15 (1, 1, 1, 1) is the minimum gain. As will be discussed in detail in Sect. 5, G0, G1 (0, 0, 0, 1), G4 (0, 1, 0, 0), and G15 are used as the gain for each channel in this report. The gain of CSA must be adjusted by selecting SW1–SW4 so that the wave height output AOUT does not saturate. However, as C_f is changed, the feedback resistor R_f, equivalently configured with an NMOS FET, must also be changed to adjust the time constant to a constant value. In this integrator, Rf1 to Rf4, corresponding to Cf1 to Cf4, are switched. R_f, which is composed of NMOS, can change the equivalent resistance by controlling the gate voltage with the external control voltage VGG. However, the noise generated by the integrator at circuit temperature T is 4kT/R_f, where k is Boltzmann's constant. Therefore, the contribution of thermal noise can be reduced by increasing R_f. The response function T of the integrator output is expressed by

$$T(s) = \frac{R_f}{1 + sC_f R_f} \cdot \left(\frac{1}{R_p} + sC_p \right) \tag{3}$$

using the Laplacian s. Although there are poles in the front-end circuit and zeros in the rear-end circuit, these can be eliminated by setting $C_f R_f = C_p R_p$ and using pole-zero cancellation.

The shaper at the entrance of the timing detector is a low-pass filter for waveform shaping. Adjusting the shaping time allows the pulse waveform to be shaped in such a way that the leading and tail decaying time constants of the waveform are equal. One of the two split signals after the shaper

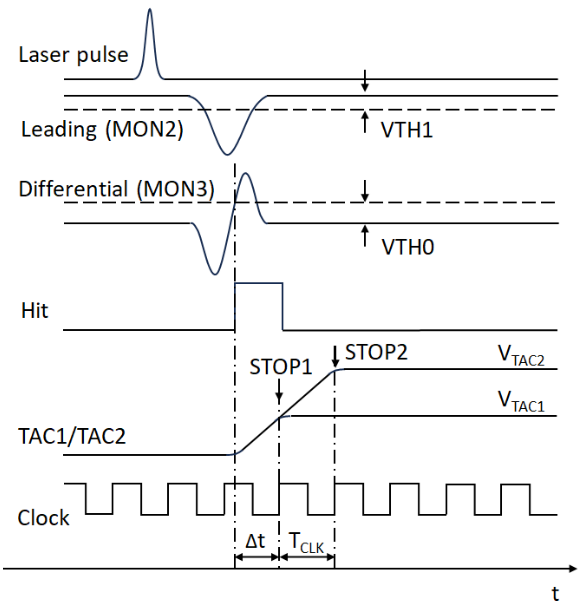

Fig. 3 Waveforms involved in timing measurements. Leading and Differential are internal signals of the CSA. The HIT signal is a digital output indicating detection timing. TAC1 and TAC2 are internal signals of the TAC. Clock is an external counter digital clock.

is a signal waveform referred to as "Leading," and the other is converted to a bipolar waveform by the differential circuit, referred to as "Differential." The signal detection timing is the moment that Leading signal has the peak voltage when Differential voltage becomes zero during the period while Leading exceeds VTH1. Figure 3 shows the main signal waveforms and their timings. The SW is ON and the voltage of Leading is connected to the capacitor before charge input from AIN. When Leading exceeds VTH1, the upper comparator outputs H that enables the lower comparator, which digitally outputs the HIT signal when Differential exceeds the threshold VTH0 (zero crossing) during the period while Leading exceeds VTH1. Then, the following D flip-flop (DFF) outputs H as DSUM as the detection timing signal. At the same time the DFF outputs L from $\overline{\mathrm{Q}}$ which turns off the SW to store the Leading voltage at that moment as AOUT in the capacitor of the peak hold circuit. AOUT is an analog-level output, and it is read with an external AD converter. Additionally, the HIT signal triggers the TAC circuit described in Sect. 3.4. Offset adjustment of Leading and Differential is very important and can be set by the built-in DAC. Leading and the Differential can be output externally as MON2 and MON3 waveforms for measurement.

The input terminal AIN of the CSA module can be fed with a charge pulse input from the test terminal TP via the capacitor Ctp. Specifically, a pulse charge Qtp = Ctp · Vtp can be input by inputting a step voltage Vtp from the TP terminal. This allows the CSA to be electrically checked without using the optical input.

3.4 Time-to-Analog Converter

If a high-frequency digital clock is used to achieve the required distance resolution of about 10 cm, then a clock of 1 GHz or higher is required. Consequently, relying only on high-frequency clocks produces difficulties for device selection, board design, and power consumption for spacecraft. For this reason, LIDARX is equipped with a clock interpolator and uses a clock as low as 20 MHz to achieve sub-nanosecond resolution.

LIDARX has two identical TAC circuits, which are shown in Fig. 1. The TAC is a circuit that outputs a voltage proportional to time (sawtooth wave) when triggered by an HIT signal from a CSA and stops the voltage increase by inputting the external digital signal STOP. The STOP signal uses a clock that drives an external time measurement counter. The clock can be interpolated by reading the analog outputs VTAC1 and VTAC2 from the TAC. The HIT and TAC timing waveforms are shown in Fig. 3. TAC1 and TAC2 start outputting sawtooth waves with a slope of approximately 3 to 4 mV/ns triggered by HIT. The timing to stop the sawtooth wave are STOP1 and STOP2, which have an offset of 1 CLK. Therefore, since the voltage difference between the analog voltages VTAC1 and VTAC2 corresponds to the clock period TCLK, the voltage slope (VTAC2 − VTAC1)/TCLK can be obtained. The interpolation time Δt can then be obtained from the voltage slope and VTAC1 using

$$\Delta t = \frac{T_{CLK}}{V_{TAC2} - V_{TAC1}} \cdot V_{TAC1}. \tag{4}$$

There is no strict specification for the frequency of the clock that controls the stopping of the TAC, so a clock of about 20 MHz is used to achieve the required distance resolution of about 10 cm. The start and stop of the TAC sawtooth wave are accompanied by a delay, but since the delays are fixed, the accuracy of the measurement is not affected. However, the interpolation performance of the TAC is strongly dependent on circuit noise and AD converter performance.

3.5 Output and Monitoring Functions

As mentioned previously, the detection timing of the input pulses is output digitally as HIT and its latch signal DSUM, as well as the analog signals TAC1 and TAC2 for interpolation. The wave height of the pulses is also output in analog form as AOUT. MONOUT is a pin that switches the internal signals MON0–MON3 and outputs them as analog waveforms. The output signal from MONOUT is switched by an external digital input.

Although the details have been omitted for conciseness, channel switching, gain switching, time constant adjustment, offset adjustment in the IC, and output signal switching can be controlled by digital input to the registers. The registers used for these settings consist of shift registers using radiation-tolerant dual-interlocked storage-cell flip-flops (DICE-FFs) and can be set via the serial interface.

4. Evaluation Apparatus

The apparatus that used optical pulse input to evaluate the

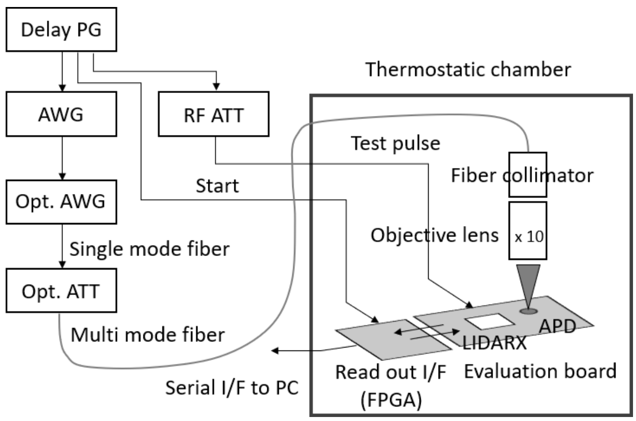

Fig. 4 Schematic of the evaluation apparatus.

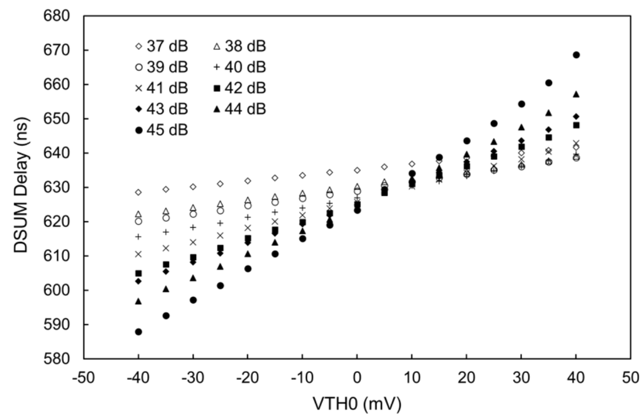

Fig. 5 Optimization of VTH0.

function and performance of this device is shown in Fig. 4. The LIDARX evaluated in this device is a bare chip from the same manufacturing rod as the flight model (FM), and it was mounted in a ceramic package for testing purposes. The circuits and components used on the evaluation board are commercially available but were selected with application to the FM in mind. The APD mounted on the board is an industrial-level product (Excelitas C30954EH) of the same type as that used in the FM. The evaluation board is temperature-controlled in a thermostatic chamber to obtain the temperature characteristics, and the digital values set in LIDARX and its output data are written or read by a personal computer via a read-out I/F board with a field-programmable gate array (FPGA) mounted. The FPGA also implements the digital control functions of a normal LIDAR, including functions for generating timing signals such as the range counter, counter clock, and start and end of ranging. Analog values such as AOUT and TAC generated by LIDARX are digitized by the ADC on the evaluation board, read by the FPGA, and sent to the PC.

The measurement is triggered by the start pulse output by the delay pulse generator to the read out I/F. The delay pulse generator sends a trigger pulse to the arbitrary waveform generator (AWG), and the AWG outputs a voltage pulse to the optical AWG, which is the source of the optical pulse shape. In this apparatus, the TOF is measured as the total time required for the 900 ns laser firing delay by the delay pulse generator and for the laser to reach the APD from the laser diode. Although the optical AWG can reproduce the output waveform of an actual laser pulse, a Gaussian waveform with a wave height of 1.0 V and a full width at half maximum of 10 ns is used in this study for the sake of generality. The wavelength of the laser diode used in the optical AWG is 1064 nm, the same as the fundamental wave of a YAG laser. The optical pulses are input into a multimode fiber by a collimation lens and transmitted into a thermostatic chamber after the output is adjusted (0 to 69 dB) by an optical attenuator combined with an ND filter. The light pulses are injected into the APD by the collimation lens and objective lens in the thermostatic chamber. The diameter of the light footprint on the surface of the APD is 0.15 mm, which is small enough for the 0.8 mm diameter of the APD's sensitive area. The transmittance of the optical system with optical attenuator and fiber is 69.2%. When the AWG outputs a 1-V, 10-ns Gaussian waveform with an ATT = 0 dB setting, 1.25 nJ of light energy is incident on the APD.

When the temperature of the APD is 25°C and the operation voltage is 360 V, the APD multiplication factor M = 120 and the quantum efficiency η = 36% [27] for a wavelength of 1064 nm. Therefore, the photoelectron charge Q for 1.25 nJ of light energy is Q = 49 nC, which is obtained from

$$Q = \frac{E_{pulse} \cdot M \cdot \eta}{h\nu} \cdot e, \tag{5}$$

where ν, E_{pulse}, and h are the optical frequency (Hz), optical pulse energy (J), and Planck constant (J · s), respectively.

As described in Sect. 3.3, LIDARX has a function that allows charge pulses to be input directly to the CSA by means of a step voltage input from the test pulse terminal. In this case, the pulse voltage from the delay pulse generator is adjusted to an appropriate voltage by an RF attenuator and input from the test pulse terminal.

5. Calibration

5.1 Optimization of Detection Thresholds

As explained in Sect. 3, the IC determines the arrival timing of light pulses when Differential exceeds the threshold value VTH0. Therefore, VTH0 is an important threshold value that directly affects detection accuracy. Additionally, the dependence of the detection timing on the input light level to the APD (i.e., the amount of charge input to the IC) must be kept as low as possible. Figure 5 shows the optimal VTH0 using CH1 G15 as a specific example. The vertical axis shows the delay from the reference timing of the detection timing DSUM measured with an oscilloscope, and the horizontal axis shows the threshold VTH0. The optical input level is adjusted between 37 and 44 dB by the optical attenuator of the evaluation system (Fig. 4). Figure 5 shows

Table 1 Cubic curve coefficients for approximating DSUM delay.

Ch.	VTH0	Coefficients				MAE
	mV	x^3	x^2	x^1	x^0	ns
0	5	66.011	-119.33	88.50	602.89	0.07
1	5	-11.97	45.61	-25.04	632.13	0.04
2	30	-10.26	33.64	-21.49	650.60	0.14
3	30	5.00	16.379	-15.18	634.79	0.09
4	20	428.34	-384.22	-126.95	597.59	0.03

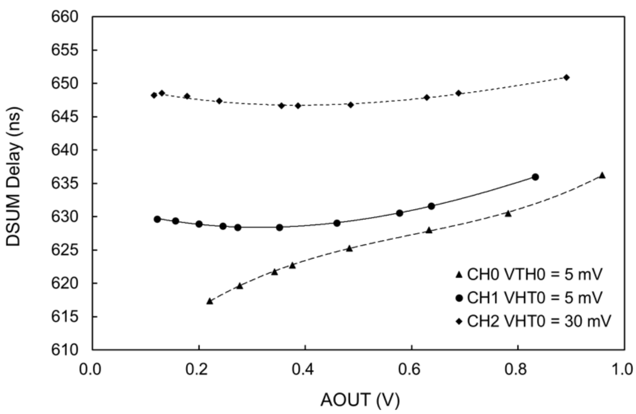

Fig. 6 Approximating DSUM delay with a cubic curve.

that the VTH0 at which the DSUM delay distribution becomes small is around 5 to 10 mV. When the optimal VTH0 is selected, the DSUM delay remains a fixed delay that is inherent to each CH, with a gain and slight variation due to the amount of input charge. In an actual LIDAR system, LIDARX can estimate the input charge in terms of the wave height AOUT. Because the DSUM delay needs to be estimated from AOUT, it is convenient if the DSUM delay can be approximated by a polynomial of AOUT. In this work, the optimal value of VTH0 is selected as the threshold value at which the approximation curve with the smallest error is obtained. A third-order polynomial is used for the approximation curve, and the error is evaluated by the mean absolute error (MAE) given by

$$MAE = \frac{1}{n}\sum_{i=1}^{n} |y_i - \widehat{y}_i|, \tag{6}$$

where y_i is the measured value, $\widehat{y}_i$ is the predicted value, and n is the number of data points. The optimal thresholds and polynomial coefficients for G15 for CH0–CH4 at 25°C are presented in Table 1. Figure 6 shows the relationship between wave height AOUT and DSUM delay for CH0, CH1, and CH2 in Table 1. In distance measurements using LIDAR, the DSUM delay on the vertical axis is obtained from the AOUT value on the horizontal axis using the approximation formula in Table 1. Since LIDAR onboard the MMX is an observation device, the estimation of delay using this approximation curve is performed by a ground-based computer.

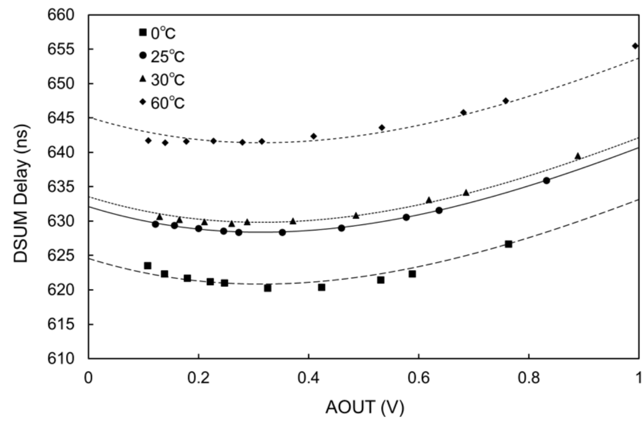

Fig. 7 Temperature dependence of the DSUM delay.

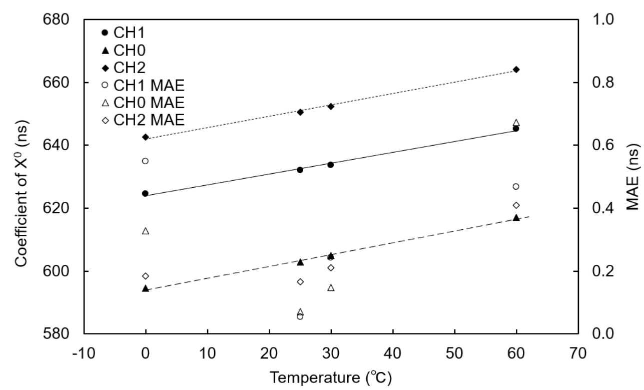

Fig. 8 Temperature dependence of the X^0 coefficient of the cubic curve.

5.2 Thermal Characteristics

Transistor operation is generally temperature-dependent, and LIDARX is no exception. Figure 7 shows the AOUT dependence of the DSUM delay at CH1 G15, measured from 0°C to 60°C. For 25°C, the data are the same as those for CH1 in Fig. 6. The delay increased as the temperature increased from 0°C to 60°C, which is consistent with the characteristic that transistors generally operate faster at lower temperatures. From Fig. 7, it can be seen that the effect of temperature appears as an offset in the curve, so the approximate curve measured at 25°C can be approximated by translating the curve along the vertical axis. Specifically, this can be solved by making the constant X^0, shown in Table 1, a linear function of temperature. The constant X^0 and MAE for CH0, CH1, and CH2 for G15 are shown in Fig. 8. All of the channels show a linear temperature dependence. Additionally, MAE, which is used as an evaluation criterion, exhibited no significant degradation at 25°C for any of the channels.

All channels use a common TAC circuit to interpolate the clock, as shown in Fig. 1. We have already observed that the TAC slope $(V_{TAC2} - V_{TAC1})/T_{CLK}$ in Eq. (4) also has a temperature dependence, with the characteristic that the TAC slope is larger the lower the temperature. However, based on the TAC design, the temperature dependence is not a problem

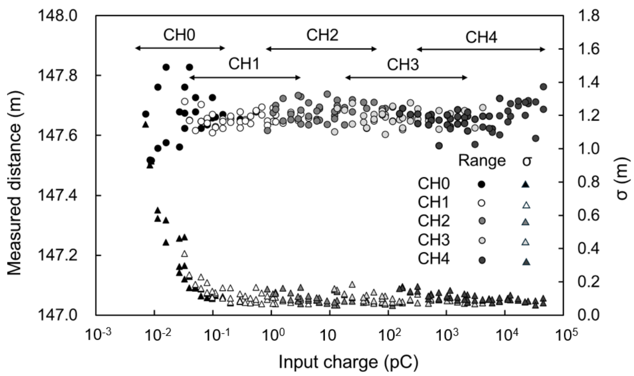

Fig. 9 Distance measurement accuracy. Channels are differentiated based on concentration, not gain.

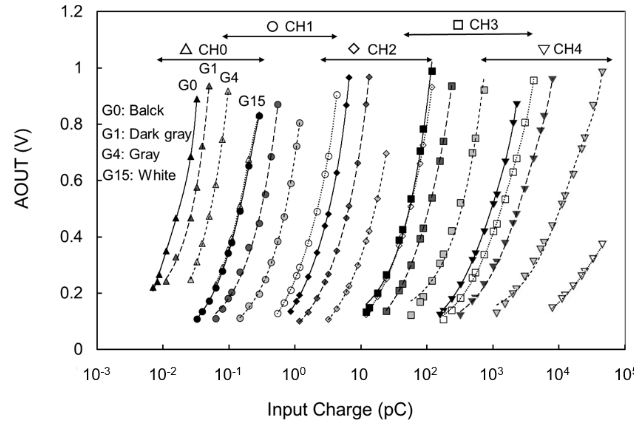

Fig. 10 Relationship between the input charge and the AOUT output. The shape of the marker represents the channel, and the color represents the gain.

for two reason. Firstly, the two TAC circuits are of the same design on the same chip, so their temperature characteristics can be regarded as identical. Secondly, V_{TAC1} and V_{TAC2} can calibrate the TAC slope for each pulse detection operation.

6. Distance and Wave Height Measurement

6.1 Distance Measurement Accuracy

The LIDARX calibration method was introduced in Sect. 5. When using the system, all channel and gain combinations must be calibrated. We calibrated five channels (CH0–CH4) for G0, G1, G4, and G15, for a total of 20 combinations, using Gaussian waveform light pulses with a 10-ns pulse width. Figure 9 shows the results of distance measurements using LIDARX after calibration, again at 25°C with a 10-ns pulse width Gaussian waveform. The vertical axis is the measured distance, which is a fixed distance determined by the delay of the delay pulse generator of the evaluation device shown in Fig. 4. The horizontal axis is the amount of charge input from the APD to LIDARX corresponding to the optical input adjusted by the optical attenuator shown in Fig. 4. The results show that the distance measurement results are concentrated at 147.7 m ± 0.1 m. The standard deviation of the measurement is also about 0.1 m, indicating sufficient accuracy. However, the distance measurement results for input charges below 100 fC show that the range of the distribution extends to about ±0.2 m, and the standard deviation also deteriorates from 0.2 m to 1.2 m. However, this region can be concluded to have sufficiently high accuracy because it is the region for long-distance measurements over several tens of kilometers in actual LIDAR measurements.

6.2 Wave Height Measurement

The measured wave height AOUT from the experiment in Fig. 9 is shown in Fig. 10. The range of input charges is the same as in Fig. 9. For CH1 to CH4 we can see that a single channel and gain combination has a dynamic range of about 10 to 12 dB, and the AOUT corresponding to the input is measured in the range from 0.1 to 1.0 V. For CH0, the dynamic range of one gain is rather narrow, at about 8 dB, and the corresponding AOUT output ranges from 0.2 to 0.8 V. Therefore, the input CH and CSA gain (switches SW1–SW4) must be switched by the external control to keep the wave height output AOUT in the range 0.2–0.8 V for CH0 and 0.1 V to 1.0 V for CH1–CH4. In orbital measurements, the dynamic range of each channel and gain must have sufficient overlap because the distance to the target object changes over time. The minimum gain of CH0 and the maximum gain of CH1 almost overlap. The maximum gain of CH1 and the minimum gain of CH2 also have sufficient overlap. Therefore, a combination of five channels and four gains can be used to ensure continuous measurement in the 60-dB input charge range from fC to nC. Additionally, automatic gain control of LIDAR can be performed by controlling the channels and gains of LIDARX to keep the AOUT in the appropriate range.

7. Radiation Tolerance

7.1 Total Ionizing Dose

The total ionizing dose (TID) [28] for the entire mission period of MMX is assumed to be 20 krad in the silicon equivalent, assuming shielding with 1 mm of aluminum. We performed γ-ray irradiation tests with 60Co at the National Institutes for Quantum Science and Technology. The ceramic package was placed in an aluminum case with its lid open, and gamma irradiation was performed with the IC power supply turned on. The irradiation rate was 1 krad/h, and a maximum dose of 24 krad was tested. Post-irradiation measurements were taken twice, once within 24 h and again after 1 month. The measurement after 1 month took annealing into account. The tests were evaluated in terms of wave height AOUT and distance values considering DSUM delay and TAC interpolation. Before and after γ-ray irradiation, the change in DSUM delay was less than 0.5 m in distance conversion, and the AOUT change was less than 10 mV. No changes in leakage current and current consumption were also measured. Considering this result, LIDARX was determined to be tolerant to a TID of up to 24 krad. When implemented in the LIDAR system, LIDARX has an equivalent aluminum shielding thickness of more than 1 mm and a low dose rate, so it can be concluded that the use of LIDARX in the MMX mission will not be a problem.

7.2 Single-Event Effects

Single-event effects (SEEs) are phenomena that cause temporary malfunctions or permanent failures due to transient currents generated by the charge produced by the ionization effect of energetic particles, such as protons or heavy ions, when they strike semiconductor devices. In LIDARX, single-event upsets (SEUs) [29] and single-event latch-ups (SELs) [30] are the most problematic SEEs. The internal FFs that perform channel selection, gain adjustment, and offset voltage adjustment are affected by SEUs and should be investigated. Two types of FFs are used in LIDARX: the D (data) type and the DICE type with high inversion tolerance.

Especially important information for ranging, such as gain and threshold voltage settings, are stored only in DICE-FFs. Heavy ion beams accelerated by the AVF cyclotron at the National Institutes for Quantum Science and Technology were used to test SEE resistance. Five types of heavy ion beams, namely, N (40 MeV), Ne (54 MeV), Ar (107 MeV), Kr (230 MeV), and Xe (350 MeV), were used to evaluate the SEE tolerance at five levels of linear energy transfer (LET) (MeV-cm^2/mg). In this test, the beam directly irradiated the bare LIDARX chip in a vacuum chamber. SEU generation was detected by monitoring the FF readout. SEL was detected by monitoring the current consumption of the device.

It is generally known that the relationship between LET and the scattering cross-section σ can be approximated by the Weibull curve [31]

$$\sigma = \sigma_o \left\{ 1 - \exp\left(- \left| \frac{L - L_o}{W} \right| \right)^s \right\}, \qquad (7)$$

where L is the effective LET (MeV-cm^2/mg), L_0 is the LET threshold, σ_0 is the plateau cross-section (cm^2/bit), and S and W (MeV-cm^2/mg) are the Weibull coefficients. The SEU cross-sections and fitted Weibull curves from heavy ion irradiation are shown in Fig. 11. However, SEUs from D-FF irradiation with Ne and DICE-FF irradiation with Ar were not measured, so the fitting curves were calculated assuming a single inversion.

The parameters obtained by fitting were input into CREME96 [32] to estimate the on-orbit SEU occurrence rate, and the results showed that the SEU rates for DICE-FF and D-FF were less than 10^{-5} per day. Therefore, it can be concluded that the likelihood of SEU occurrence during the six-year MMX mission is very low. For SELs, we confirmed that they do not occur even when LIDARX is heated to 80°C and irradiated with Xe, which has the highest LET, at a sufficient fluence (> 3.54×10^7 p/cm^2). Consequently, it can be assumed that latch-ups due to particles with an LET

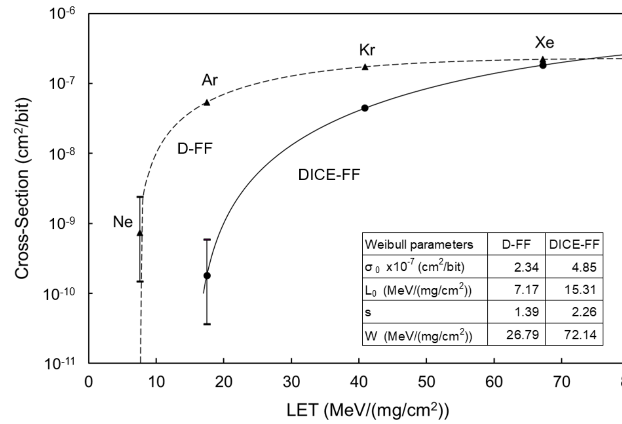

Weibull parameters	D-FF	DICE-FF
σ_0 x10^{-7} (cm^2/bit)	2.34	4.85
L_0 (MeV/(mg/cm^2))	7.17	15.31
s	1.39	2.26
W (MeV/(mg/cm^2))	26.79	72.14

Fig. 11 Measurement of the SEU cross-section using heavy ions. The error bars show the 68% confidence interval for the Poisson distribution.

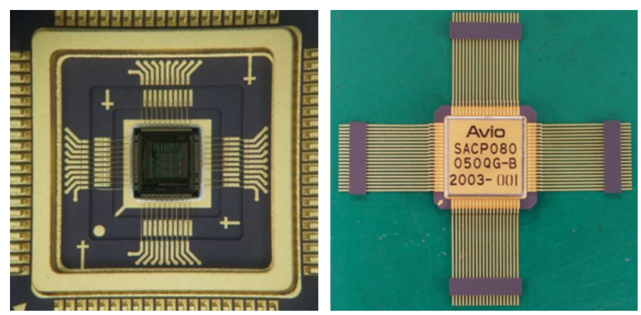

(a) Before sealing. (b) Top view of package.

Fig. 12 The FM package of LIDARX.

of 65 MeV/(mg/cm^2) or less of Xe do not occur.

8. Packaging

The FM product is a bare chip mounted in the 80-pin metal package shown in Fig. 12. The quality of this IC is equivalent to Class 2. Quality conformance inspection and screening tests were conducted by MIL-STD-883 for the items specified in JAXA-QTS-2010. The electrical characteristics were divided into DC characteristics, AC characteristics, and functional test items. For DC characteristics, test items included current consumption, various reference voltages, leakage voltage of the digital input section, and output voltage of the digital output section. The test pulse function of LIDARX was used to test the AC characteristics. The specified pulses were input from the test pulse pin, and the delay time to the DSUM output, Leading and Differential waveforms as intermediate signals in the IC, wave height AOUT, and TAC slope were inspected. The functions tested included offset adjustment using the internal DAC and the ability to adjust the threshold values VTH0 and VTH1.

As a typical test example, an operating life test of 1000 h at 125°C and a temperature cycle life test of 100 temperature cycles from −55°C to 150°C were conducted to confirm that there were no problems. During the screening, all individuals were subjected to a burn-in at 125°C for 240 h.

9. Conclusion

The optical pulse detection IC LIDARX was developed for use in LIDAR receivers onboard planetary probes. This IC has the functions of timing detection, wave height measurement, and clock interpolation. Furthermore, it has a wide dynamic range of 60 dB with respect to light intensity to accommodate distance changes of about three orders of magnitude, which is expected when LIDAR is used as a navigation sensor during landing. This report describes the details, functions, and calibration method of the peripheral circuits of LIDARX and the circuits inside the IC, and provides an overview of its dynamic range and measurement accuracy using an experimental device for evaluation. The TID tolerance was 24 krad and latch-up-free in terms of radiation resistance, which is essential for onboard spacecraft components. The reliability of this IC is equivalent to Class 2.

Based on the experience of LIDAR development for the asteroid probes Hayabusa and Hayabusa2, we have developed LIDARX to have better performance, a shorter development period, and more stable performance. We expect that this IC will be utilized for planetary exploration, especially landing-based exploration employing LIDAR, including the MMX mission.

Acknowledgments

We thank D. Tokiwa and Y. Aonuma of the Graduate School of Tokai University for their efforts in radiation tests of this device and for data processing. We also thank M. Kawano for her contribution to the manufacturing of experimental printed circuit boards used in the development of this device.

References

[1] S. Nozette, P. Rustan, L.P. Pleasance, J.F. Kordas, I.T. Lewis, H.S. Park, R.E. Priest, D.M. Horan, P. Regeon, C.L. Lichtenberg, E.M. Shoemaker, E.M. Eliason, A.S. McEwen, M.S. Robinson, P.D. Spudis, C.H. Acton, B.J. Buratti, T.C. Duxbury, D.N. Baker, B.M. Jakosky, J.E. Blamont, M.P. Corson, J.H. Resnick, C.J. Rollins, M.E. Davies, P.G. Lucey, E. Malaret, M.A. Massie, C.M. Pieters, R.A. Reisse, D.E. Smith, T.C. Sorenson, R.W. Vorder Breugge, and M.T. Zuber, "The clementine mission to the moon: Scientific overview," Science, vol.266, no.5192, pp.1835–1839, 1994.

[2] L. Ramos-Izquierdo, J.L. Bufton, and P. Hayes, "Optical system design and integration of the Mars observer Laser altimeter," Applied Optics, vol.33, no.3, pp.307-322, 1994.

[3] T.D. Cole, "NEAR laser rangefinder: A tool for the mapping and topologic study of asteroid 433 Eros," Johns Hopkins APL Technical Digest, vol.19, no.2, pp.142–157, 1998.

[4] M.T. Zuber, D.E. Smith, A.F. Cheng, and T.D. Cole, "The NEAR laser ranging investigation," Journal of Geophysical Research: Planets, vol.102, no.E10, pp.23761–23773, 1997.

[5] J.F. Cavanaugh, J.C. Smith, X. Sun, A.E. Bartels, L. Ramos-Izquierdo, D.J. Krebs, J.F. McGarry, R. Trunzo, A.M. Novo-Gradac, J.L. Britt, J. Karsh, R.B. Katz, A.T. Lukemire, R. Szymkiewicz, D.L. Berry, J.P. Swinski, G.A. Neumann, M.T. Zuber, and D.E. Smith, "The mercury laser altimeter instrument for the MESSENGER mission," Space Science Reviews, vol.131, no.1-4, pp.451–479, 2007.

[6] S.C. Solomon, R.L. McNutt Jr., R.E. Gold, and D.L. Domingue, "MESSENGER mission overview," Space Science Reviews, vol.131, no.1-4, pp.3–39, 2007.

[7] H. Noda, H. Araki, S. Goossens, Y. Ishihara, K. Matsumoto, S. Tazawa, N. Kawano, and S. Sasaki, "Illumination conditions at the lunar polar regions by KAGUYA (SELENE) laser altimeter," Geophysical Research Letters, vol.35, no.24, 2008.

[8] H. Araki, S. Tazawa, H. Noda, Y. Ishihara, S. Goossens, S. Sasaki, N. Kawano, I. Kamiya, H. Otake, J. Oberst, C. Shum, "Lunar global shape and polar topography derived from Kaguya-LALT laser altimetry," Science, vol.323, no.5916, pp.897–900, 2009.

[9] W. Xu, Y. Hongxuan, H. Jiang, P. Tong, Y. Kuang, M. Li, and R. Shu, "Navigation Doppler lidar sensor for precision landing of China's Chang'E-5 lunar lander," Applied Optics, vol.59, no.27, pp.8167–8174, 2020.

[10] H. Zhang, J. Li, Z. Wang, and Y. Guan, "Guidance navigation and control for Chang'E-5 powered descent," Space: Science & Technology, vol.2021, 9823609, 2021.

[11] A.J. George, "A short review on India's interplanetary missions," Acceleron Aerospace Journal, vol.2, no.1, pp.138–147, 2024.

[12] D.A. Lorenz, R. Olds, A. May, C. Mario, M.E. Perry, E.E. Palmer, and M. Daly, "Lessons learned from OSIRIS-REx autonomous navigation using natural feature tracking," 2017 IEEE Aerospace Conference, Big Sky, MT, USA, pp.1–12, 2017.

[13] C.S. Dickinson, M.C. Daly, O. Barnouin, B. Bierhaus, D. Gaudreau, J. Tripp, M. Ilnicki, and A.R. Hildebrand, "An overview of the OSIRIS REx laser altimeter - OLA," 43rd Lunar and Planetary Science Conference, 1447, 2012.

[14] M.G. Daly, O.S. Barnouin, C. Dickinson, J. Seabrook, C.L. Johnson, G. Cunningham, T. Haltigin, D. Gaudreau, C. Brunet, I. Aslam, A. Taylor, E.B. Bierhaus, W. Boynton, M. Nolan, and D.S Lauretta, "The OSIRIS-REx laser altimeter (OLA) investigation and instrument," Space Science Reviews, vol.212, no.1-2, pp.899-924, 2017.

[15] E. Church, T. Bourbeau, J. Curriden, A. Deguzman, F. Jaen, H. Ma, K. Mahoney, C. Miller, B. Short, K. Waldorff, O. Walthall, and D. Lauretta, "Flash lidar on-orbit performance at asteroid bennu," Proc. 43rd Annual AAS Guidance, Navigation and Control Conference, pp.20–148, 2020.

[16] A. Dietrich and J.W. McMahon, "Orbit determination using flash lidar around small bodies," Journal of Guidance, Control, and Dynamics, vol.40, no.3, pp.650–665, 2017.

[17] T. Mizuno, K. Tsuno, E. Okumura, and M. Nakayama, "Evaluation of LIDAR system in rendezvous and touchdown sequence of Hayabusa mission," Trans. Japan Society for Aeronautical and Space Science, vol.53, no.179, pp.47–53, 2010.

[18] T. Mizuno, T. Kase, T. Shiina, M. Mita, N. Namiki, H. Senshu, R. Yamada, H. Noda, H. Kunimori, N. Hirata, F. Terui, and Y. Mimasu, "Development of the laser altimeter (LIDAR) for Hayabusa2," Space Science Reviews, vol.208, no.1-4, pp.33–47, 2016.

[19] T. Hashimoto, T. Kubota, and T. Mizuno, "Light weight sensors for the autonomous asteroid landing of MUSES-C mission," Acta Astronautica, vol.52, no.2-6, pp.381–388, 2003.

[20] S. Watanabe, Y. Tsuda, M. Yoshikawa, S. Tanaka, T. Saiki, and S. Nakazawa, "Hayabusa2 mission overview," Space Science Reviews, vol.208, no.1-4, pp.3–16, 2017.

[21] T. Mizuno, H. Ikeda, and K. Kawahara, "Development of a ROIC for lidar on planetary lander by CMOS technology," Proc. SPIE 8379, Laser Radar Technology and Applications XVII, vol.8379, 837910, 2012.

[22] K. Asada, T. Nakura, T. Iizuka, and M. Ikeda, "Time-domain approach for analog circuits in deep sub-micron LSI," IEICE Electron. Express, vol.15, no.6, 20182001, 2018.

[23] O. Kumagai, J. Ohmachi, M. Matsumura, S. Yagi, K. Tayu, K. Amagawa, T. Matsukawa, O. Ozawa, D. Hirono, Y. Shinozuka, R. Homma, K. Mahara, T. Ohyama, Y. Morita, S. Shimada, T. Ueno, A. Matsumoto, Y. Otake, T. Wakano, and T. Izawa, "7.3 A 189 × 600 back-illuminated stacked SPAD direct time-of-flight depth sensor for

automotive LiDAR systems," 2021 IEEE International Solid-State Circuits Conference (ISSCC), San Francisco, CA, USA, pp.110–112, 2021.

[24] K. Yoshioka, H. Kubota, T. Fukushima, S. Kondo, T.T. Ta, H. Okuni, K. Watanabe, M. Hirono, Y. Ojima, K. Kimura, S. Hosoda, Y. Ota, T. Koizumi, N. Kawabe, Y. Ishii, Y. Iwagami, S. Yagi, I. Fujisawa, N. Kano, T. Sugimoto, D. Kurose, N. Waki, Y. Higashi, T. Nakamura, Y. Nagashima, H. Ishii, A. Sai, and N. Matsumoto, "A 20-ch TDC/ADC hybrid architecture LiDAR SoC for 240 × 96 pixel 200-m range imaging with smart accumulation technique and residue quantizing SAR ADC," IEEE J. Solid-State Circuits, vol.53, no.11, pp.3026–3038, Nov. 2018.

[25] K. Kuramoto, Y. Kawakatsu, M. Fujimoto, A. Araya, M.A. Barucci, H. Genda, N. Hirata, H. Ikeda, T. Imamura, J. Helbert, S. Kameda, M. Kobayashi, H. Kusano, D.J. Lawrence, K. Matsumoto, P. Michel, H. Miyamoto, T. Morota, H. Nakagawa, T. Nakamura, K. Ogawa, H. Otake, M. Ozaki, S. Russell, S. Sasaki, H. Sawada, H. Senshu, S. Tachibana, N. Terada, S. Ulamec, T. Usui, K. Wada, S. Watanabe, and S. Yokota, "Martian moons exploration MMX: Sample return mission to Phobos elucidating formation processes of habitable planets," Earth, Planets and Space, vol.74, 12, https://doi.org/10.1186/s40623-021-01545-7, 2021.

[26] H. Senshu, T. Mizuno, K. Umetani, T. Nakura, A. Konishi, A. Ogawa, H. Ikeda, K. Matsumoto, H. Noda, Y. Ishihara, S. Sasaki, N. Tateno, Y. Ikuse, K. Mayuzumi, T. Kase, and H. Kashine, "Light detection and ranging (LIDAR) laser altimeter for the Martian Moons Exploration (MMX) spacecraft," Earth, Planets and Space, vol.73, 219, 2021.

[27] Excelitas_Si_APD_C30954EH_datasheet, https://www.excelitas.com/product/c30954eh-si-apd-08mm-5-package

[28] H.J. Barnaby, "Total-ionizing-dose effects in modern CMOS technologies," IEEE Trans. Nucl. Sci., vol.53, no.6, pp.3103–3121, 2006.

[29] R. Baumann, "Soft errors in advanced computer systems," IEEE Des. Test, vol.22, no.3, pp.258–266, 2005.

[30] P.E. Dodd and L.W. Massengill, "Basic mechanisms and modeling of single-event upset in digital microelectronics," IEEE Trans. Nucl. Sci., vol.50, no.3, pp.583–602, 2003.

[31] J. Barak, "Simple calculations of proton SEU cross sections from heavy ion cross sections," IEEE Trans. Nucl. Sci., vol.53, no.6, pp.3336–3342, 2006.

[32] CREME Site, https://creme.isde.vanderbilt.edu/

Takahide Mizuno is a professor in the sensors and microdevices field at the Institute of Space and Astronautical Science (ISAS), JAXA. He is interested in ranging devices for onboard spacecraft and is currently working on Flash LIDAR for G&NC. He has led the development of LIDAR for navigation and scientific observation onboard the asteroid explorers Hayabusa and Hayabusa2, contributing to their successful landing on the asteroid and sample acquisition.

Hirokazu Ikeda received a Ph.D. in physics from the University of Tokyo in 1978. He joined KEK in Tsukuba in 1978 before moving to ISAS, JAXA in 2005. His research interest covers IC design as well as fundamental physics. He is now an emeritus professor of JAXA.

Hiroki Senshu is a principal staff scientist at Chiba Institute of Technology, Japan. He received a Doctor of Science in Thermal Evolution Theory of Mars from the University of Tokyo in 2001. He is a member of Hayabusa2, Hera, and MMX missions. He is a co-I of LIDAR onboard Hayabusa2 and the PI of LIDAR onboard MMX.

Toru Nakura was born in Fukuoka, Japan in 1972. He received the B.S., and M.S. degree in electronic engineering from The University of Tokyo, Tokyo, Japan, in 1995 and 1997 respectively. Then he worked as a circuit designer of high-speed communication using SOI devices for two years, and worked as a EDA tool developer for three years. He joined the University of Tokyo again as a Ph.D. student in 2002, and received the degree in 2005. After two years industrial working period, he is back to academia as an associate professor at VLSI Design and Education Center (VDEC), and Electrical Engineering and Information Systems, in The University of Tokyo. He is now currently working as an full professor in the department of Electronics Engineering and Computer Science in Fukuoka University. His current interest includes signal integrity, reliability, power supply, digitally-assisted analog circuits, and fully automated analog circuit synthesis.

Kazuhiro Umetani received the M. and Ph.D. degrees in geophysical fluid dynamics from Kyoto University, Kyoto, Japan in 2004 and 2007, respectively. In 2015, he received a second Ph.D. degree in electrical engineering from Shimane University, Japan. From 2007 to 2008, he was a Circuit Design Engineer for Toshiba Corporation, Japan. From 2008 to 2014, he was with the Power Electronics Group in DENSO CORPORATION, Japan. From 2014 to 2020, he was an Assistant Professor at Okayama University, Okayama, Japan. From 2020 to 2021, he was an Associate Professor at Tohoku University, Miyagi, Japan. From 2021, he is currently an Associate Professor at Okayama University, Okayama, Japan. His research interests include new circuit configurations in power electronics and power magnetics for vehicular applications.

Akihiro Konishi received a B.S. degree from the National Institute of Technology, Nara College (NITNC), Nara, Japan, in 2017, and the M.S. and Ph.D. degrees in electrical engineering from Okayama University, Okayama, Japan, in 2019 and 2023, respectively. He has been engaged as a project assistant professor at Chiba University, Chiba, Japan, since 2023. His research interests include a wireless power transfer system and the design of a controller for a high-frequency switching circuit.

Akihito Ogawa participated in research at JAXA (ISAS) from 2017 to 2019, focusing on the adaptability of LIDARX to space environments. Based on his research findings, he obtained a Master's degree in Mechanical Engineering from Tokai University in 2019. Since 2019, he has been working on research and development related to space development at IHI Aerospace Corporation, a subsidiary of IHI Corporation in Japan.

Kaito Kasai graduated from the Department of Aeronautics and Astronautics at Tokai University's Faculty of Engineering in 2024. He is currently pursuing a Master's degree in Mechanical Engineering at the Graduate School of Engineering, Tokai University, where his research focuses on the application of LIDAR technology.

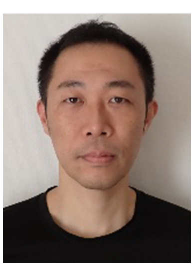

Kosuke Kawahara is an associate senior engineer in the Institute of Space and Astronautical Science (ISAS), JAXA. He has been engaged in the development and operation of tracking radars for the sounding rocket. He was led the sample return capsule (SRC) recovery operation team for Hayabusa and Hayabusa2 and contributed to the successful recovery of the SRCs.